



Interfacial instability of thin ferrofluid films under a magnetic field

Ivana Seric, Shahriar Afkhami[†] and Lou Kondic

Department of Mathematical Sciences, New Jersey Institute of Technology,
Newark, NJ 07103, USA

(Received 8 May 2014; revised 18 June 2014; accepted 23 July 2014)

We study magnetically induced interfacial instability of a thin ferrofluid film subjected to an applied uniform magnetic field and covered by a non-magnetizable passive gas. Governing equations are derived using the long-wave approximation of the coupled static Maxwell and Stokes equations. The contact angle is imposed via a disjoining/conjoining pressure model. Numerical simulations show the patterning resulting from unstable perturbations and dewetting of the ferrofluid film. We find that the subtle competition between the applied field and the van der Waals induced dewetting determines the appearance of satellite droplets. The results suggest a new route for generating self-assembled ferrofluid droplets from a thin film using an external magnetic field. An axisymmetric droplet on a surface is also studied, and we demonstrate the deformation of the droplet into a spiked cone, in agreement with experimental findings.

Key words: breakup/coalescence, magnetic fluids, thin films

1. Introduction

Thin liquid films are ubiquitous in nature and also appear in many technological applications. An understanding of their dynamical behaviour and their stability is therefore of great importance and has consequently attracted considerable attention in the literature. Recent advances in studying thin-film flows have resulted in developments in experimental and theoretical research in this field, including the manipulation of thin-film flows via the use of external magnetic or electric fields to produce nanoscale patterns. In particular, experiments on thin ferrofluid films have shown the formation of a wide range of morphologies (Dickstein *et al.* 1993; Chen & Cheng 2008; Chen & Li 2010). Ferrofluids consist of magnetic nanoparticles in a colloidal solution that can be manipulated using magnetic forces, and have been extensively investigated and widely used in a variety of engineering applications; see Rosensweig (1987) and a more recent review by Nguyen (2012).

[†] Email address for correspondence: shahriar.afkhami@njit.edu

Thin films driven by an electric field have been extensively studied in the past; see e.g. Shankar & Sharma (2004), Craster & Matar (2005), Yeo, Craster & Matar (2007) and Roberts & Kumar (2009, 2010). Based on the earlier work of Shankar & Sharma (2004), Craster & Matar (2005) derive a coupled system of evolution equations for the interfacial location and charge density using the long-wave theory. They consider the dynamics of two thin films of leaky dielectric fluids sandwiched between two infinitely long, rigid and impermeable electrodes. The stability of liquid bilayers (see e.g. Roberts & Kumar 2009) and trilayers (see e.g. Roberts & Kumar 2010) under an AC electric field has also been investigated. The long-wave approximation of a thin film under an electric field has been used to study the drop manipulation in the work by Yeo *et al.* (2007). They include the effects of the van der Waals force using a disjoining pressure model. The flow of ferrofluid films under an external magnetic field is governed by a similar dynamics to leaky dielectric liquid films in an electric fields. However, with the number of their applications growing, surprisingly, little can be found in the literature on the long-wave approximation of thin ferrofluid films.

In this work, we derive a model for the flow of a thin ferrofluid film on a substrate in the same spirit as the previous work by Shankar & Sharma (2004) and Craster & Matar (2005) for the case of a leaky dielectric model. The derivation for a non-conducting ferrofluid simplifies since there is no interfacial charge involved. We also extend this model in order to account for the van der Waals force and to impose the contact angle using the disjoining/conjoining pressure model (see e.g. Diez & Kondic 2007), enabling us to study, for the first time, the film breakup and the deformation of sessile droplets on the substrate under an external magnetic field. We solve the resulting evolution equation numerically and show that the results are in full agreement with the linear stability analysis. The growing unstable perturbations result in breakup of the thin film into primary droplets. We have found that, depending on the strength of the magnetic force compared with the van der Waals force, satellite (secondary) droplets can also form.

A recent study has shown that a ferrofluid droplet on a hydrophobic substrate breaks up into two daughter droplets and a smaller satellite droplet under a sufficiently strong magnetic field (Timonen *et al.* 2013*b*). These experiments also show that if the magnetic field is increased even further, the droplets break up again and rearrange to form an assembly of droplets on the substrate. As we will see below, our simulations also reveal satellite droplets, although the model that we develop includes only a subset of the physical effects present in the experiments. We find satellite droplets even for wetting surfaces, and show that they appear only for a sufficiently strong magnetic field. Finally, motivated by recent experimental results (Malouin, Vogel & Hirs 2010; Malouin *et al.* 2011), we also simulate the deformation of an axisymmetric drop on a substrate, again by considering a simplified set-up that allows us to focus only on the main features of the influence of the magnetic field on the droplet shape. While previous works considered ferrofluid drops travelling through a viscous medium (Afkhami *et al.* 2008) and a deformation of a suspended ferrofluid drop (Afkhami *et al.* 2010), we are unaware of studies reporting simulations of the dynamics of a ferrofluid drop on a surface.

2. Model

We use the long-wave approximation to derive a two-dimensional model from Stokes equations coupled with the static Maxwell equations. Figure 1 shows the schematic of the system of two thin fluid films in the region $0 < y < \beta h_c$, with the

Interfacial instability of thin ferrofluid films

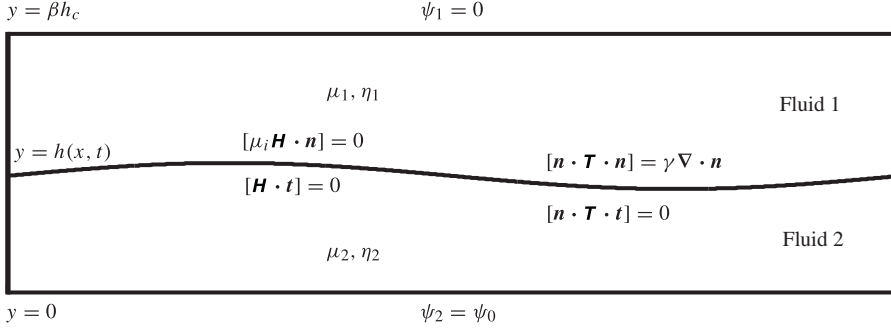


FIGURE 1. The schematic of the system of two thin fluids, where fluid 1 is non-magnetic and fluid 2 is ferrofluid.

ferrofluid film occupying the region $0 < y < h_c$ and the non-magnetic fluid occupying the rest of the domain. We denote the permeability and viscosity of the fluids by μ_i and η_i , where $i = (1, 2)$ denotes fluids 1 and 2, respectively. The interface between two fluids is denoted by $y = h(x, t)$.

The magnetic field satisfies the static Maxwell equations, $\nabla \cdot \mathbf{B} = 0$ and $\nabla \times \mathbf{H} = 0$, where \mathbf{B} is the magnetic flux and \mathbf{H} is the magnetic field, related by $\mathbf{B} = \mu_i \mathbf{H}$. The permeabilities of the non-magnetic fluid and the ferrofluid are $\mu_1 = \mu_0$ and $\mu_2 = \mu_0 (1 + \chi_m)$, respectively, where χ_m is the magnetic susceptibility and $\mu_0 = 4\pi \times 10^{-7} \text{ N A}^{-2}$ is the permeability of the surrounding fluid, approximated by the permeability of vacuum. The magnetic scalar potential, ψ , satisfies $\mathbf{H} = \nabla \psi$, which together with the Maxwell equations implies

$$\nabla^2 \psi_i = 0. \quad (2.1)$$

The boundary conditions at the bottom and top boundaries are $\psi(0, t) = \psi_0$ and $\psi(\beta h_c, t) = 0$. At the interface, $y = h(x, t)$, the normal component of \mathbf{B} and the tangential component of \mathbf{H} are continuous, $[\mu_i \mathbf{H} \cdot \mathbf{n}] = 0$ and $[\mathbf{H} \cdot \mathbf{t}] = 0$, where \mathbf{n} and \mathbf{t} , are the unit normal and tangential vectors to the interface, respectively, given by

$$\mathbf{n} = \frac{1}{(1 + h_x^2)^{1/2}} (-h_x, 1), \quad \mathbf{t} = \frac{1}{(1 + h_x^2)^{1/2}} (1, h_x). \quad (2.2a,b)$$

Given the small thickness of fluids, we ignore inertial effects and gravity. Hence, the equations governing the motion of the fluids are Stokes equations for continuity and momentum balance, $\nabla \cdot \mathbf{u}_i = 0$, $\nabla \cdot \mathbf{T}_i = 0$, respectively, where \mathbf{u}_i is the velocity and $\mathbf{T}_i = -p_i \mathbf{I} + \boldsymbol{\Sigma}_i + \mathbf{M}_i + \Pi \mathbf{I}$ is the total stress tensor. Here, p_i is the isotropic pressure, $\boldsymbol{\Sigma}_i = \eta_i (\nabla \mathbf{u}_i + \nabla \mathbf{u}_i^T)$ is the viscous stress tensor for a Newtonian fluid, $\mathbf{M}_i = \mu_i [H_i H_i - (1/2) (H_i \cdot H_i) \mathbf{I}]$ is the Maxwell stress tensor and the disjoining pressure is specified by

$$\Pi(h) = \bar{\kappa} f(h), \quad \text{where } f(h) = (h_*/h)^n - (h_*/h)^m. \quad (2.3)$$

Here, $\bar{\kappa} = \gamma \tan^2 \theta / (2Mh_*)$ and $M = (n - m) / [(m - 1)(n - 1)]$. In this form, Π includes the disjoining/conjoining intermolecular forces due to van der Waals

interactions, which is commonly used in the literature (see e.g. Diez & Kondic 2007). The prefactor $\bar{\kappa}$, which can be related to the Hamaker constant, measures the strength of van der Waals forces. Here, γ is the surface tension and h_* is the short length scale introduced by the van der Waals potential. A variety of values of the exponents (n, m) can be found in the literature (see e.g. Diez & Kondic 2007). We use (3, 2) and have verified that consistent results are obtained when choosing other commonly used exponents, such as (4, 3) and (9, 3). The contact angle, θ , is the angle at which the fluid/fluid interface meets the substrate.

Since the divergence of the Maxwell stress tensor is zero inside each fluid and $\nabla \Pi = 0$ except at the interface, the conservation of momentum becomes

$$-\nabla p_i + \eta_i \nabla^2 \mathbf{u}_i = 0. \quad (2.4)$$

At the top and bottom boundaries, no-slip and no-penetration conditions are imposed. At the interface $y = h(x, t)$, the boundary conditions are the continuity of the normal and tangential components of the velocity, the normal stress balance, the continuity of the shear stress and the kinematic boundary condition,

$$[\mathbf{u} \cdot \mathbf{n}] = 0, \quad [\mathbf{u} \cdot \mathbf{t}] = 0, \quad (2.5a,b)$$

$$[\mathbf{n} \cdot \mathbf{T} \cdot \mathbf{n}] = \gamma \nabla \cdot \mathbf{n}, \quad [\mathbf{n} \cdot \mathbf{T} \cdot \mathbf{t}] = 0, \quad (2.6a,b)$$

$$h_t + u_2 h_x = v_2, \quad (2.7)$$

respectively, where $\nabla \cdot \mathbf{n}$ is the interfacial curvature. Since $[\mathbf{n} \cdot \mathbf{M} \cdot \mathbf{t}] = 0$, the continuity of the tangential component of the stress can be written as $[\mathbf{n} \cdot \boldsymbol{\Sigma} \cdot \mathbf{t}] = 0$.

2.1. Scalings

Next, we non-dimensionalize the governing equations and boundary conditions as follows (dimensionless variables are denoted by a tilde):

$$x = x_c \tilde{x}, \quad (y, h) = h_c (\tilde{y}, \tilde{h}), \quad \delta = h_c/x_c, \quad u = u_c \tilde{u}, \quad v = (\delta u_c) \tilde{v}, \quad (2.8a-e)$$

$$p = (\eta_2 u_c x_c / h_c^2) \tilde{p}, \quad t = (x_c / u_c) \tilde{t}, \quad \psi_i = \psi_0 \tilde{\psi}_i, \quad (2.9a-c)$$

where $\delta \ll 1$, h_c is the initial thickness of the ferrofluid film, and u_c and x_c are the characteristic velocity and horizontal length scale, respectively, given by

$$u_c = \frac{\mu_0 \psi_0^2}{\eta_2 x_c}, \quad x_c = \left(\frac{\gamma h_c^3}{\mu_0 \psi_0^2} \right)^{1/2}. \quad (2.10a,b)$$

Here, we drop the tilde notation for simplicity. In the remaining part of the paper, all variables are non-dimensional unless stated otherwise.

2.2. Evolution equation

Using the above scalings, and the assumption that $\delta \ll 1$, (2.1) and the corresponding boundary conditions for the potential are, to the leading order in δ ,

$$\psi_{i,yy} = 0, \quad (2.11)$$

$$\psi_1 = 0 \quad \text{at } y = \beta, \quad \psi_2 = 1 \quad \text{at } y = 0, \quad (2.12a,b)$$

$$\psi_1 = \psi_2, \quad \text{and} \quad \mu_1 \psi_{1,y} - \mu_2 \psi_{2,y} = 0 \quad \text{at } y = h(x, t). \quad (2.13a,b)$$

Interfacial instability of thin ferrofluid films

Integrating (2.11) twice and using (2.12) and (2.13) to find the integration constants, the magnetic potential in each fluid is

$$\psi_1 = \mu_r c_3(x, t)(y - \beta), \quad \psi_2 = c_3(x, t)y + 1, \quad \text{where } c_3(x, t) = \frac{1}{h(\mu_r - 1) - \beta\mu_r}. \quad (2.14a, b)$$

Here, $\bar{\mu}_r = \mu_2/\mu_0$. The governing equations are, to the leading order in δ ,

$$u_{ix} + v_{iy} = 0, \quad (2.15)$$

$$-p_{1x} + \eta_r u_{1yy} = 0, \quad -p_{2x} + u_{2yy} = 0, \quad (2.16a, b)$$

$$p_{iy} = 0, \quad (2.17)$$

where $\eta_r = \eta_1/\eta_2$. The leading-order boundary conditions at $y = h(x, t)$ are

$$-p_2 + p_1 - \Pi + \frac{\mu_r}{2}\psi_{2,y}^2 - \frac{1}{2}\psi_{1,y}^2 = h_{xx}, \quad (2.18)$$

$$u_{2,y} - \eta_r u_{1,y} = 0. \quad (2.19)$$

The kinematic boundary condition, (2.7), remains unchanged. If we assume that the upper fluid is inviscid with constant pressure (e.g. air), we can simplify the derivation. Integrating (2.16) twice and applying the no-slip boundary condition together with (2.19) gives

$$u_2 = \frac{1}{2}p_{2x}(y^2 - 2hy), \quad (2.20)$$

where the pressure gradient p_{2x} is given by differentiating (2.18) with respect to x ,

$$-p_{2x} - \Pi_x + \frac{1 - \mu_r}{2\mu_r} [c_3^2]_x = h_{xxx}. \quad (2.21)$$

Using the kinematic boundary condition, (2.7), which can be written as $h_t + (\int_0^h u_2 dy)_x = 0$, and (2.20) and (2.21), the evolution equation for $h(x, t)$ then becomes

$$h_t + \frac{1}{3} \frac{1}{x^\alpha} \frac{\partial}{\partial x} \left[\kappa f'(h) x^\alpha h^3 h_x - \frac{\mu_r (\mu_r - 1)^{-1}}{\left(h - \frac{\beta\mu_r}{\mu_r - 1}\right)^3} h^3 x^\alpha h_x + x^\alpha h^3 \frac{\partial}{\partial x} \left(\frac{1}{x^\alpha} \frac{\partial}{\partial x} (x^\alpha h_x) \right) \right] = 0, \quad (2.22)$$

where $\kappa = h_c \gamma \tan^2 \theta / (2\mu_0 \psi_0^2 M h_*)$ is a non-dimensional parameter representing the ratio of the van der Waals to the magnetic force, and $\alpha = 0, 1$ for Cartesian and cylindrical coordinates, respectively. The ratio $\beta\mu_r/(\mu_r - 1)$ is inversely proportional to the magnetic force (it should be noted that β is the non-dimensional distance between the plates with constant potential, so the gradient of the potential is inversely proportional to β). Unless specified differently, the parameters used in the simulations are $\kappa = 13.5$, $\beta = 8$, $\mu_r = 44.6$ and $h_* = 0.01$. These parameters correspond to values of γ and μ_2 for an oil-based ferrofluid ($\gamma = 0.034 \text{ N m}^{-1}$, $\mu_2 = \mu_0(1 + \chi_m)$, where $\chi_m = 3.47 \times 4\pi$) and $\psi_0 = 1.2 \text{ A}$, and β is chosen to produce a sufficiently strong magnetic field.

We note that, aside from the inclusion of the van der Waals term, the evolution equation (2.22) is of the same form as derived for the leaky dielectric model by Shankar & Sharma (2004) and Craster & Matar (2005) in the absence of interfacial charges and in the limit of the viscosity ratio approaching zero. The addition of the van der Waals forces is crucial in the present context, since it allows us to study dewetting of thin films as well as to investigate the deformation of sessile droplets under a magnetic field. We discuss these problems next.

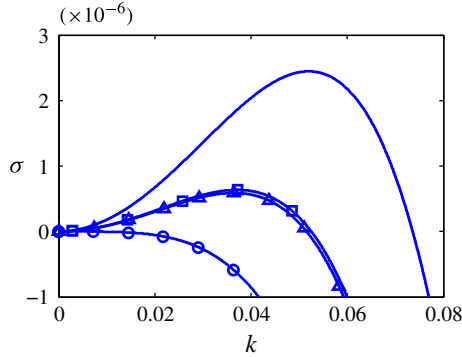


FIGURE 2. The effect of each term in the dispersion relation, (3.1), for $h_0 = 1$. The plain solid line shows the dispersion curve for $\kappa = 13.5$, $\beta = 8$, $\mu_r = 44.6$ and $h_* = 0.01$ (we use these parameters throughout except if specified differently). The lines with squares and triangles are obtained by excluding the effect of the van der Waals ($\kappa = 0$) and magnetic force ($\mu_r = 1$), respectively, and the line with circles corresponds to the results obtained in the presence of surface tension only ($\kappa = 0$ and $\mu_r = 1$).

3. Results

In this section, we present the results of the linear stability analysis (LSA) as well as the fully nonlinear time-dependent simulations of the evolution equation (2.22). We consider two problems. In § 3.2, we discuss the evolution of a perturbed flat film that, if unstable, leads to film breakup and results in the formation of primary and satellite droplets. In § 3.3, we consider the evolution of an axisymmetric drop on a substrate.

3.1. Linear stability analysis

We carry out an LSA of the evolution equation (2.22), for $\alpha = 0$, by perturbing the flat film around the constant thickness h_0 , so that $h(x, t) = h_0 + \varepsilon h_0 e^{ikx + \sigma t}$, where $\varepsilon \ll h_0$ is the amplitude of the perturbation. The dispersion relation to $O(\varepsilon)$ is

$$\sigma = -\frac{h_0^3 k^2}{3} [k^2 - k_c^2], \quad \text{where } k_c = \left[\kappa \left(-n \frac{h_*^n}{h_0^{n-1}} + m \frac{h_*^m}{h_0^{m-1}} \right) - \frac{\mu_r (\mu_r - 1)^2}{(h_0 (\mu_r - 1) - \beta \mu_r)^3} \right]^{1/2}. \quad (3.1)$$

We note that (3.1) is equivalent to the dispersion relation derived in Pease & Russel (2002) for the case of a perfect dielectric in the absence of the van der Waals interactions. Figure 2 shows a typical dispersion curve with $h_0 = 1$. There is a range of wavenumbers, $0 < k < k_c$, for which the growth rate σ is positive, and therefore the perturbations will be unstable. We can see from figure 2 that both the magnetic and the van der Waals terms have a destabilizing effect. For the present choice of parameters, both the van der Waals and the magnetic terms have a similar effect, at least on the level of LSA.

3.2. Numerical simulations: evolution of a film

The computational methods that we use are based on a finite-difference approach outlined in Kondic (2003). The Crank–Nicolson time stepping scheme is used combined with the Newton method for solving the resulting system of nonlinear

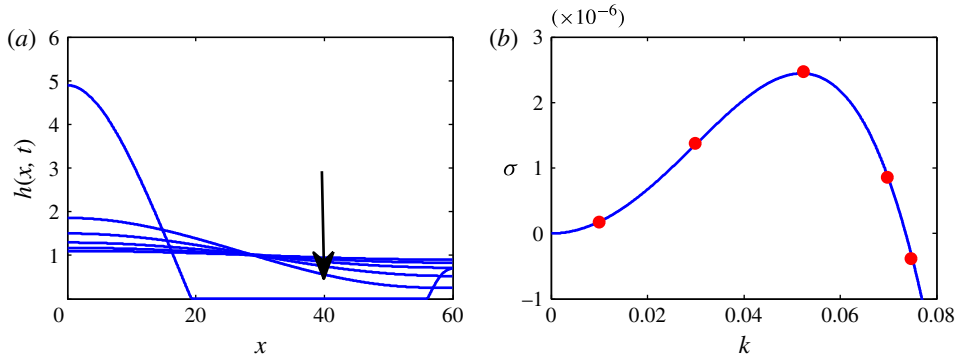


FIGURE 3. (a) Evolution of a flat film of thickness $h_0 = 1$ and amplitude of perturbation $\epsilon = 0.1$, perturbed by the most unstable wavenumber, k_m . The arrow indicates the direction of increasing time. (b) Comparison of the predicted values of the growth rate from the LSA (solid line) with values obtained from the numerical simulations (circles).

algebraic equations obtained by spatial discretization. The grid size is chosen equal to h_* and the time step is variable and based on accuracy requirements. We have verified that the numerical results are fully converged and, furthermore, we have validated them by comparing with the LSA, as outlined below. The initial condition is set to a flat film perturbed around a constant thickness h_0 , i.e. $h(x, 0) = h_0 + \epsilon \cos(k_m x)$, with $\epsilon = 0.1$, and $h_0 = 1$. Here, k_m is the fastest growing mode computed from (3.1). Making use of the symmetry of the problem, the computational domain is chosen to be equal to one half of the wavelength of the perturbation, i.e. $L_x = \pi/k_m$. No-flux boundary conditions are imposed at the left and the right end boundaries as $h' = h''' = 0$.

Figure 3(a) shows the film evolution. As expected from the LSA, the perturbation grows in time and the film breaks up into droplets as the unstable mode grows. The large primary droplet appears at the left end point and the (secondary) satellite droplet forms at half of the wavelength. We note that even if the film drop thickness becomes relatively large and approaches the upper boundary ($\beta = 8$), the assumptions of the model are not violated, as long as the assumptions entering the implemented long-wave approximation are satisfied. From the simulations, we can calculate the growth rate by assuming that the amplitude behaves as $A(t) = A_0 e^{\sigma t}$, then σ can be obtained from the values of the amplitude found in the simulations. Figure 3(b) shows the full agreement of the numerical results with the prediction of the LSA given by (3.1).

Next, we examine the steady-state profiles obtained for a range of parameter values, in particular for the non-dimensional parameters β and κ . The former is inversely proportional to the strength of the magnetic field and the latter gives the ratio of the van der Waals force to the magnetic force. Figure 4(a) shows the comparison of the steady-state profiles for varying the parameter κ while keeping β fixed, with the initial condition the same as given above. We note that as κ decreases, i.e. the magnetic force increases compared with the van der Waals force, the satellite droplets start to appear. Similar behaviour is observed in figure 4(b) for decreasing values of β ; we observe the formation of satellite droplets for sufficiently small β , i.e. the magnetic field dominates over the van der Waals interaction. It should also be noted that the satellite droplets are not present in the simulations where the effect of the magnetic field is ignored (when $\mu_r = 1$). We also note that for $\beta = 7.0$ shown in figure 4(b),

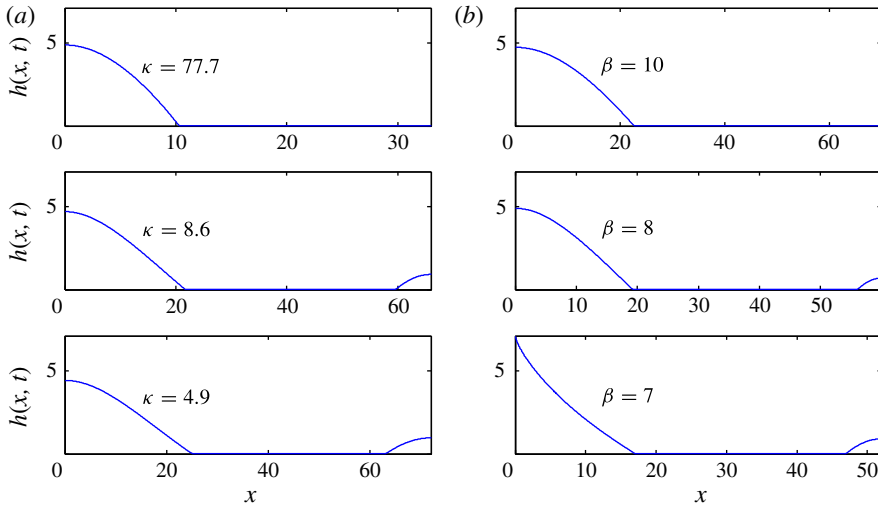


FIGURE 4. The effect of varying β and κ on the film evolution with $h_* = 0.01$ when (a) $\beta = 8$ is fixed and (b) $\kappa = 13.5$ is fixed. It should be noted that when $\beta \leq 7.0$, no steady-state drop profile can be achieved, indicative of an interfacial instability, as also discussed in the text.

a static drop cannot be obtained, unlike when $\beta > 7.0$: here, the height of the fluid approaches the top boundary and the assumptions of the model are not satisfied for times later than the one at which this profile is shown.

In order to better understand the mechanism leading to the formation of satellite droplets, we consider the LSA of the film (we call it a ‘bridge’) between the primary drops. Figure 5(a) shows the film profiles as the satellite droplet starts to form, i.e. when the height of the film at $x = L_x/2$ starts to increase. To investigate the stability of the bridge, we fit (half) cosine waves to the film profile, as illustrated in the inset of figure 5(a). The symbols (\times) indicate the beginning and the end of these (half) cosine waves. Figure 5(b) shows the phase plot in (h_0, k_c) space, in both the presence and the absence of the magnetic field. Here, the circles correspond to the thickness of the bridge shown in figure 5(a) with the direction of increasing time indicated by the arrow. We see that the bridge stability changes from stable to unstable while passing through the region where instabilities occur only when the magnetic field is present. Our results therefore suggest that the magnetically induced instability of the bridge that forms between primary drops could be a reason for the formation of the satellite droplets. In order to better understand the dynamics of the primary drop retraction after the breakup, we also show in figure 5(a) the droplet evolution just before and after the liquid bridge breaks up. As shown, the evolution of the drop after the breakup occurs on a very rapid time scale.

Figure 6 shows a phase plot in $(\kappa, \beta\mu_r/(\mu_r - 1))$ space, presenting the influence of κ and $\beta\mu_r/(\mu_r - 1)$ on the formation of the satellite droplets. Both of these dimensionless variables are inversely proportional to the strength of the magnetic field. The values of parameters where the satellite droplets are present (absent) are represented by the solid blue (hollow red) symbols. We see that the appearance of the satellite droplets depends only on the values of κ and $\beta\mu_r/(\mu_r - 1)$. This finding gives a way of predicting (and controlling) the resulting morphologies for ferrofluid films for a range of physical parameters, such as surface tension, equilibrium contact angle, magnetic susceptibility and initial film thickness.

Interfacial instability of thin ferrofluid films

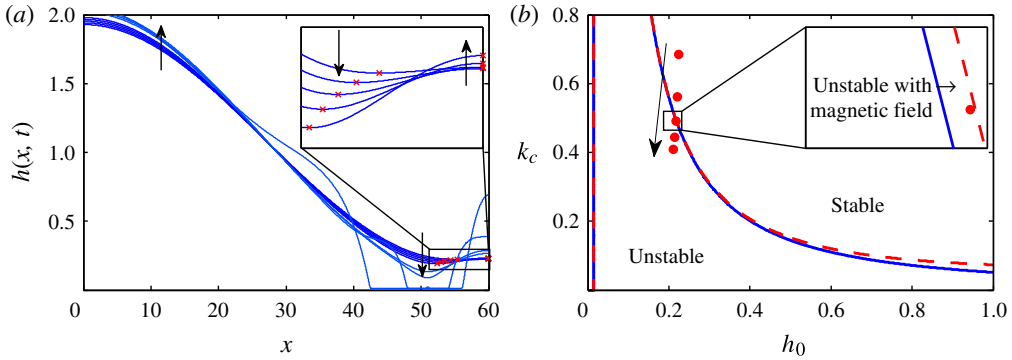


FIGURE 5. Stability of the bridge that forms between primary droplets. (a) Film profiles as the satellite droplets start to form just before and after the liquid bridge breaks up. The symbols (\times) indicate the beginning and the end of one half of the cosine wavelength that we fit to the numerical results at various times. The arrows indicate the direction of increasing time. The time interval between each profile is 5×10^3 time units (dimensionless). The inset shows the zoomed-in region at the right boundary. (b) The regions of stability: red (dashed) and blue (solid) lines correspond to $\mu_r = 44.6$ and $\mu_r = 1$, respectively. The symbols correspond to the values for the bridge thickness measured at the times shown in (a). The arrow indicates the direction of increasing time. The inset shows the region where the bridge transitions from stable to unstable, while passing through the region where instabilities occur only when the magnetic field is present.

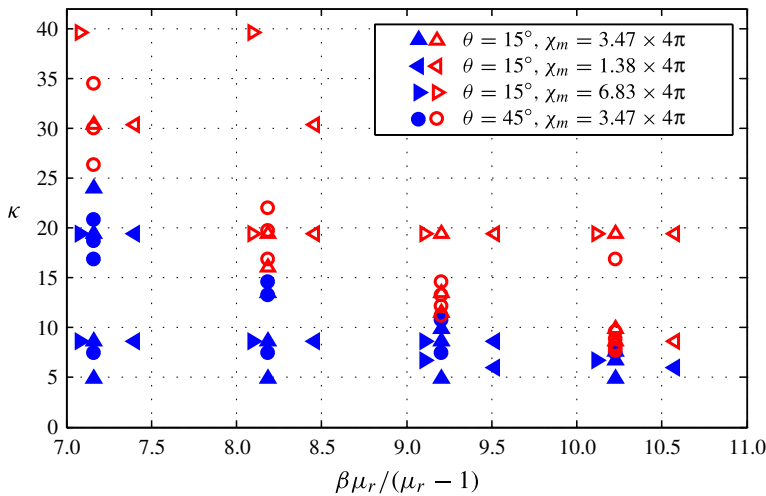


FIGURE 6. Phase diagram showing the influence of κ and $\beta\mu_r/(\mu_r - 1)$ on the formation of satellite droplets. The blue (solid) symbols represent the parameters where satellite droplets appear and the red (hollow) symbols represent the parameters where no satellite droplets form. Different symbol shapes correspond to simulations with different contact angles and magnetic susceptibilities, as indicated in the legend.

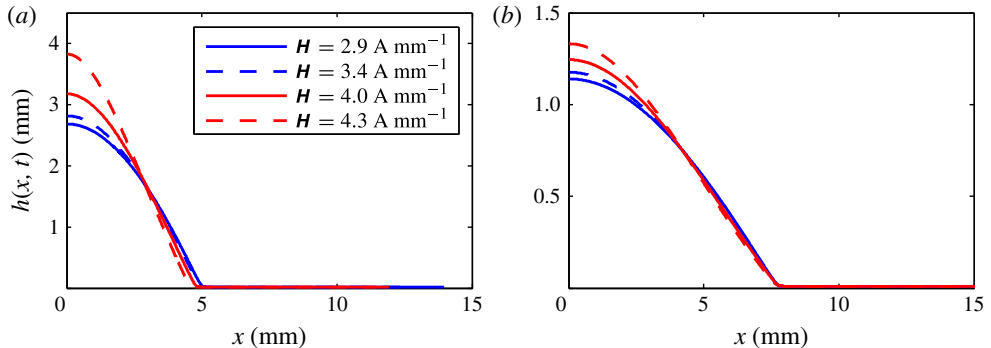


FIGURE 7. Steady-state drop profiles for varying values of magnetic field, \mathbf{H} , for a 100 mm^3 drop with an equilibrium contact angle $\theta = 45^\circ$ (a) and $\theta = 15^\circ$ (b); $h_* \approx 0.02 \text{ mm}$, $\gamma = 0.034 \text{ N m}^{-1}$ and $\chi_m = 3.47 \times 4\pi$.

3.3. Numerical simulations: axisymmetric ferrofluid drop on a substrate

Next, we consider the evolution of an axisymmetric ferrofluid drop. This problem is relevant in particular for applications in adaptive optics and has been considered in recent experiments (Malouin *et al.* 2010, 2011). Here, we consider a simplified geometry, also ignore the effects due to magnetic field gradients and discuss the coupling of magnetic field and a ferrofluid drop in a simplified setting. The initial condition is a steady-state profile obtained by imposing an equilibrium contact angle, θ , and evolving a spherical cap surrounded by a film of thickness h_* in the absence of the magnetic field. The precursor film thickness, h_* (the short length scale introduced by the van der Waals potential), is much thinner than the initial height of the droplet. We verify that the numerical simulations are converged for decreasing h_* , and find that the drop profiles are independent of h_* for $h_* < 0.01$.

Figure 7 shows the steady-state drop profiles when varying the strength of the magnetic field, defined as $\mathbf{H} = \psi_0 / \beta h_c$, in the absence of a ferrofluid, for $\theta = 45^\circ$ and $\theta = 15^\circ$. We observe increased elongation of the drop as \mathbf{H} is increased, consistently with recent experiments (private communication, A. H. Hirsra 2013). Furthermore, we show that the decrease in equilibrium contact angle results in a decrease in drop elongation, as the stronger interaction of the drop with the substrate can hinder the deformation. In our simulations, we also observe a transition from a static elongated shape to an unstable one if we further increase \mathbf{H} (results are not shown here). We note that not only drop elongation, but also drop compression, has been reported in experiments by Nguyen *et al.* (2010) and Timonen *et al.* (2013a). However, these experiments may have included field gradients, which are not considered in our model.

4. Conclusions

We study the evolution of a thin ferrofluid film on a substrate in the presence of a magnetic field. We incorporate the van der Waals interactions in the model, so that we are able to consider flow configurations involving film breakup as well as time-dependent evolution of droplets. The evolution equation is derived from the Stokes equations including the Maxwell stress tensor. The magnetic field is computed by solving the static Maxwell equations. The evolution equation is studied via the

LSA as well as fully nonlinear simulations. In the linear regime, we find excellent agreement between the LSA and numerical results. In the nonlinear regime, we find that satellite drops form in simulations, but only in the presence of a magnetic field. By combining LSA of the thin film that forms between the primary droplets and the results of simulations, we find that the satellite droplets form when (i) the magnetic force is sufficiently strong and (ii) the van der Waals force is sufficiently weak, relative to the magnetic force. We identify two control parameters, κ , the ratio of the van der Waals and magnetic forces, and $\beta\mu_r/(\mu_r - 1)$, measuring the strength of the magnetic field, that govern the formation of satellite drops.

We also compute the equilibrium shapes of a ferrofluid drop on a substrate, exposed to an applied magnetic field. We find magnetically induced elongation of the drop shape with a nearly conical end and flattened sides. However, we note that a quantitative comparison of the simulations with experiments is currently lacking and leave this extension for future work.

Acknowledgements

This work was partially supported by the NSF grant nos DMS-1320037 (S.A.) and CBET-1235710 (L.K.).

References

- AFKHAMI, S., RENARDY, Y., RENARDY, M., RIFFLE, J. S. & ST. PIERRE, T. G. 2008 Field-induced motion of ferrofluid droplets through immiscible viscous media. *J. Fluid Mech.* **610**, 363–380.
- AFKHAMI, S., TYLER, A. J., RENARDY, Y., RENARDY, M., ST. PIERRE, T. G., WOODWARD, R. C. & RIFFLE, J. S. 2010 Deformation of a hydrophobic ferrofluid droplet suspended in a viscous medium under uniform magnetic fields. *J. Fluid Mech.* **663**, 358–384.
- CHEN, C.-Y. & CHENG, Z.-Y. 2008 An experimental study on Rosensweig instability of a ferrofluid droplet. *Phys. Fluids* **20**, 054105-8.
- CHEN, C.-Y. & LI, C.-S. 2010 Ordered microdroplet formations of thin ferrofluid layer breakups. *Phys. Fluids* **22**, 014105-6.
- CRASTER, R. V. & MATAR, O. K. 2005 Electrically induced pattern formation in thin leaky dielectric films. *Phys. Fluids* **17**, 032104-17.
- DICKSTEIN, A. J., ERRAMILI, S., GOLDSTEIN, R. E., JACKSON, D. P. & LANGER, S. A. 1993 Labyrinthine pattern formation in magnetic fluids. *Science* **261**, 1012–1015.
- DIEZ, J. & KONDIC, L. 2007 On the breakup of fluid films of finite and infinite extent. *Phys. Fluids* **19**, 072107-22.
- KONDIC, L. 2003 Instability in the gravity driven flow of thin liquid films. *SIAM Rev.* **45**, 95–115.
- MALOUIN, B. A., VOGEL, M. J. & HIRSA, A. H. 2010 Electromagnetic control of coupled droplets. *Appl. Phys. Lett.* **96**, 214104-3.
- MALOUIN, B. A., VOGEL, M. J., OLLES, J. D., CHENG, L. & HIRSA, A. H. 2011 Electromagnetic liquid pistons for capillarity-based pumping. *Lab on a Chip* **11**, 393–397.
- NGUYEN, N.-T. 2012 Micro-magnetofluidics: interactions between magnetism and fluid flow on the microscale. *Microfluid Nanofluid* **12**, 1–16.
- NGUYEN, N.-T., ZHU, G., CHUA, Y.-C., PHAN, V.-N. & TAN, S.-H. 2010 Magnetowetting and sliding motion of a sessile ferrofluid droplet in the presence of a permanent magnet. *Langmuir* **26**, 12553–12559.
- PEASE, L. F. III & RUSSEL, W. B. 2002 Linear stability analysis of thin leaky dielectric films subjected to electric fields. *J. Non-Newtonian Fluid Mech.* **102**, 233–250.
- ROBERTS, S. A. & KUMAR, S. 2009 AC electrohydrodynamic instabilities in thin liquid films. *J. Fluid Mech.* **631**, 255–279.
- ROBERTS, S. A. & KUMAR, S. 2010 Electrohydrodynamic instabilities in thin liquid trilayer films. *Phys. Fluids* **22**, 122102-15.

- ROSENSWEIG, R. E. 1987 Magnetic fluids. *Annu. Rev. Fluid Mech.* **19**, 437–463.
- SHANKAR, V. & SHARMA, A. 2004 Instability of the interface between thin fluid films subjected to electric fields. *J. Colloid Interface Sci.* **274**, 294–308.
- TIMONEN, J. V. I., LATIKKA, M., IKKALA, O. & RAS, R. H. A. 2013a Free-decay and resonant methods for investigating the fundamental limit of superhydrophobicity. *Nat. Commun.* **4**, 2398.
- TIMONEN, J. V. I., LATIKKA, M., LEIBLER, L., RAS, R. H. A. & IKKALA, O. 2013b Switchable static and dynamic self-assembly of magnetic droplets on superhydrophobic surfaces. *Science* **341**, 253–357.
- YEO, L. Y., CRASTER, R. V. & MATAR, O. K. 2007 Drop manipulation and surgery using electric fields. *J. Colloid Interface Sci.* **306**, 368–378.